nature communications

Article

https://doi.org/10.1038/s41467-025-59885-x

Nucleic acid spheres for treating capillarisation of liver sinusoidal endothelial cells in liver fibrosis

Received: 21 October 2024

Accepted: 8 May 2025

Wenjia Liu[1,2,3,6], **Yuting Liu**[2], **Liqiang Zhang**[2], **Liya Li**[2], **Wenguang Yang**[4], **Jia Li**[2] & **Wangxiao He**[4,5,6]

Liver sinusoidal endothelial cells (LSECs) lose their characteristic fenestrations and become capillarized during the progression of liver fibrosis. Mesenchymal stem cell (MSC) transplantation can reverse this capillarization and reduce fibrosis, but MSC therapy has practical limitations that hinder its clinical use. Here, with the help of artificial intelligence (AI), we show that MSCs secrete a microRNA (miR-325-3p) that helps restore LSEC fenestrations (tiny pores) by modulating their cytoskeleton, effectively reversing capillarization. We further develop a spherical nucleic acid (SNA) nanoparticle carrying miR-325-3p as an alternative to MSC therapy. This SNA specifically enters fibrotic LSECs via the scavenger receptor A (Scara). In three mouse models of liver fibrosis, the SNA treatment restores LSEC fenestrations, reverses capillarization, and significantly reduces fibrosis without adverse effects. Our findings highlight the potential of SNA-based therapy for liver fibrosis, paving the way for targeted nucleic acid treatments directed at LSECs and offering hope for patients.

The liver sinusoidal endothelial cells (LSEC) are indispensable for maintaining the distinctive architecture and functionality of the hepatic sinusoids, which facilitate efficient blood circulation and metabolic exchange[1]. Furthermore, these specialized endothelial cells play an indispensable role in propelling the progression of liver fibrosis[2]. Within the context of this condition, LSEC undergo a transformative process known as capillarization - relinquishing their fenestrations and sieve plate structures while adopting a more dedifferentiated and profibrogenic phenotype[3]. This phenomenon called endothelial-to-mesenchymal transition (EMT) intensifies the fibrotic mechanism by facilitating extracellular matrix component deposition and augmenting inflammatory cell recruitment[4,5]. As such, reverting LSEC's capillarization has emerged as an auspicious therapeutic approach to alleviate liver fibrosis and reinstate optimal hepatic functionality[6,7].

The transplantation of mesenchymal stem cells (MSCs) has garnered significant attention as an exceedingly promising and arguably the only valid therapeutic approach for reversing liver fibrosis[8,9]. MSCs possess remarkable immunomodulatory and regenerative properties that can effectively mitigate fibrosis through various mechanisms, including the secretion of paracrine factors and their ability to differentiate into hepatic cell types[10,11]. In recent years, an increasing body of research has revealed that MSCs possess the ability to reverse the capillarization process of LSEC, thereby reinstating fenestrae in the sinusoidal endothelium and restoring the normal structure and function of liver sinusoids[12,13]. This process of revascularization not only alleviates fibrosis but also enhances hepatic microcirculation, facilitating overall recovery of liver function[14]. Nevertheless, the clinical translation of stem cell transplantation is impeded by safety concerns such as tumorigenicity and immune rejection, ethical dilemmas associated with cell sourcing, technical complexities in differentiation and transplantation, and exorbitant costs[15,16]. Hence, revealing the underlying mechanism of MSC in reversing the capillarized LSEC and

---

[1]Department of Otorhinolaryngology Head and Neck Surgery, The Second Affiliated Hospital of Xi'an Jiaotong University, Xi'an, China. [2]Institute for Stem Cell & Regenerative Medicine, The Second Affiliated Hospital of Xi'an Jiaotong University, Xi'an, China. [3]Key Laboratory of Surgical Critical Care and Life Support (Xi'an Jiaotong University), Ministry of Education, Xi'an, China. [4]Department of Medical Oncology, The First Affiliated Hospital of Xi'an Jiaotong University, Xi'an, PR China. [5]Department of Talent Highland, The First Affiliated Hospital of Xi'an Jiaotong University, Xi'an, PR China. [6]These authors contributed equally: Wenjia Liu, Wangxiao He. e-mail: wenjialiu@xjtu.edu.cn; hewangxiao5366@xjtu.edu.cn

subsequently developing an alternative approach that can be swiftly translated into clinical practice, while ensuring utmost safety during treatment for liver fibrosis, becomes an imperative task from this point forward.

In this work, a fundamental mechanism underlying the reversal of LSEC capillarization by MSCs has been unveiled with the assistance of artificial intelligence (AI). Herein, MSCs intricately secrete miR-325-3p to modulate the cytoskeleton of LSECs, thereby reinstating their fenestrations and sieve plate structures at differentiation state. Based on this foundation, a spherical nucleic acid (SNAs) targeting LSEC was ingeniously crafted by assembling sulfhydryl and Au(I)-modified miR-325-3p into a mesmerizing spheroid polyhedron measuring approximately 39 nm through the captivating phenomenon of aurophilic interaction. Thanks to two remarkable factors: 1) the highly specific overexpression of scavenger receptor A (Scara) in hepatic fibrotic LSECs and 2) the Scara's exceptional affinity for spherical nucleic acids[17,18], SNAs selectively infiltrates into LSECs. More significantly, SNAS effectively reversed the capillarization of liver sinusoidal endothelial cells (LSEC) and exhibited remarkable therapeutic efficacy in three mouse models of liver fibrosis, encompassing oxidative stress-induced fibrosis caused by carbon tetrachloride (CCl_4), drug toxicity-induced fibrosis induced by thioacetamide (TAA), and cholestasis-derived fibrosis induced by bile duct ligation (BDL). Importantly, these beneficial effects were accompanied by a maintained favorable biosafety profile. The development and translation of this SNAs into clinical applications, so to speak, has the potential to revolutionize the management of liver fibrosis, offering newfound hope for patients suffering from chronic liver diseases.

Results

AI-assisted exploration of the reversal of LSEC capillarization by MSCs

To investigate the underlying mechanism behind the reversal of LSEC capillarization by MSCs, a sophisticated nested cell compartmentalized co-culture chamber was employed to separate physical contact between cells while maintaining a connected culture environment. Illustrated in Fig. 1A, LSEC cell line was seeded into the lower chamber, whereas MSC or its culture medium was introduced into the upper chamber. Notably, the mesenchymal stem cells (MSCs) of human origin were characterized by the expression of three positive markers (CD105, CD90, and CD29) and the absence of two negative markers (CD14 and CD31)[19], as demonstrated in Supplementary Fig. 1A. Additionally, it is important to highlight that human mesenchymal stem cells (MSCs) can mitigate liver fibrosis in mice primarily through the secretion of bioactive substances, including extracellular vesicles, proteins, and cytokines[20,21]. These substances modulate the liver microenvironment and promote tissue repair, thereby playing a pivotal role in reducing fibrotic markers and enhancing hepatocyte regeneration across species[22,23]. Consequently, human mesenchymal stem cells (MSCs) were employed in this study to treat murine liver sinusoidal endothelial cells (LSECs). Remarkably, scanning cryo-electron microscopy (Fig. 1A) captured and corresponding analysis (Fig. 1B) confirmed that mesenchymal stem cells (MSCs) and their conditioned medium (MSC-CM), isolated following a 72-hour incubation of MSCs, demonstrated the capacity to restore the fenestrations and sieve plate structures of liver sinusoidal endothelial cells (LSECs). This finding is largely consistent with the baseline controls of LSECs derived from healthy livers (Supplementary Fig. 1B). Intriguingly, this redifferentiation process could be impeded upon centrifugal removal of extracellular vesicles (MSC-CM$^{\Delta EV}$), strongly suggesting their pivotal role as active substances responsible for LSEC redifferentiation. Moreover, when RNase was added to the MSC-CM, it effectively hindered this remarkable restoration process of LSEC functionality, thereby providing compelling evidence that nucleic acids may serve as key components within these active substances.

Due to the predominant presence of miRNA in extracellular vesicles, an artificial intelligence (AI) model was developed to discern the active miRNA by collaboratively analyzing multiple omics data. Leveraging ChatGPT 4.0, this AI model underwent training through machine learning using human and mouse miRNAs along with their corresponding target genes from Gene Set Enrichment Analysis (GSEA) and TargetScan databases (Fig. 1C). Subsequently, the RNA-seq results obtained from LSECs isolated from mice with CCl_4-induced liver fibrosis, either treated with MSC or mock-treated, were inputted into this AI model to discern the active miRNA responsible for these differentially expressed genes. Similarly, the proteomics results derived from LSECs isolated from 3 healthy donors and 12 patients with cirrhosis were also incorporated into this AI model. By performing these two independent operations, the AI model respectively identified the Top 10 miRNAs most likely responsible for these differences (Fig. 1C), and interestingly, only miR-325-3p appeared in both sets of results. To further elucidate the identity of the four miRNAs, GSEA was conducted on their target genes using both proteomic data and RNA-seq data. In terms of the former, only the target genes of miR-325-3p exhibited statistically significant up-regulation in patients with cirrhosis within LSECs (Fig. 1D). Regarding mice, miR-325-3p also demonstrated a statistically significant alteration in both comparisons: between healthy LSECs and hepatic fibrosis LSECs, as well as between MSC-treated and untreated hepatic fibrosis LSECs (Fig. 1E). The collective findings suggested miR-325-3p as the pivotal agent responsible for the reversal of LSEC capillarization by MSCs.

The LSEC capillarization is reversed by MSC in a miR-325-3p-dependent manner

To validate the pivotal role of miR-325-3p, LSECs were isolated from three patients afflicted with severe liver fibrosis. Notably, these patients exhibited significantly elevated AST levels (Fig. 2A), extensive fibrotic regions (Fig. 2B, C), and a considerable degree of LSEC endothelialization (Fig. 2D and Supplementary Fig. 2A). Furthermore, the isolated LSECs exhibited a notable absence of fenestrations and sieve plate structures (Fig. 2E). This phenomenon was similarly observed in fibrotic liver tissue of mice through SEM analysis (Supplementary Fig. 2B). Remarkably, following transfection with miR-325-3p mimics using Lipo 3000 and subsequent confirmation of successful transfection by RT-PCR (Supplementary Fig. 2C), the LSECs derived from all three patients exhibited a resplendent resurgence of fenestrations and sieve plate structures within a mere 48 hours (Fig. 2E). This revival was accompanied by a remarkable augmentation in both the diameter and total count of sieve plates compared to their pre-transfection levels, as illustrated in Fig. 2F. The findings of this study unequivocally demonstrate the profound impact exerted by miR-325-3p in effectively reversing LSEC capillarization.

Next, in order to investigate the role of miR-325-3p in MSC treatment, we transfected the inhibitor of miR-325-3p (miR-325i) into the MSCs. Subsequently, we transplanted both MSCs and miR-325i-treated ones into mice with liver fibrosis induced by CCl_4. Remarkably, our findings revealed that MSC treatment significantly reduced the fibrotic area characterized by Sirius red staining in comparison to mock treatment with NaCl (Fig. 2G, H). However, this remarkable efficacy was largely attenuated when miR-325i was introduced (Fig. 2G, H). Consistent with these observations, transplantation of MSCs also led to a statistically significant decrease in α-SMA levels (a marker for active hepatic stellate cells) (Fig. 2I, J), as well as Col I level (Fig. 2K, L), while decreasing F4/80 levels (a marker for active Kupffer cells) (Fig. 2M, N) and increasing Lyve-1 levels (a marker for differentiated LSEC) (Fig. 2O, P). Conversely, miR-325i-treated MSCs did not exhibit such effects on these markers (Fig. 2I–P). Furthermore, SEM images of the isolated LSECs after MSC transplantation revealed that miR-325i block the MSC's biofunction in the reversal of LSEC capillarization (Fig. 2Q, R). Afterward, we conducted an analysis to determine the levels of miR-325-3p in MSC and isolated LSEC from hepatic fibrosis

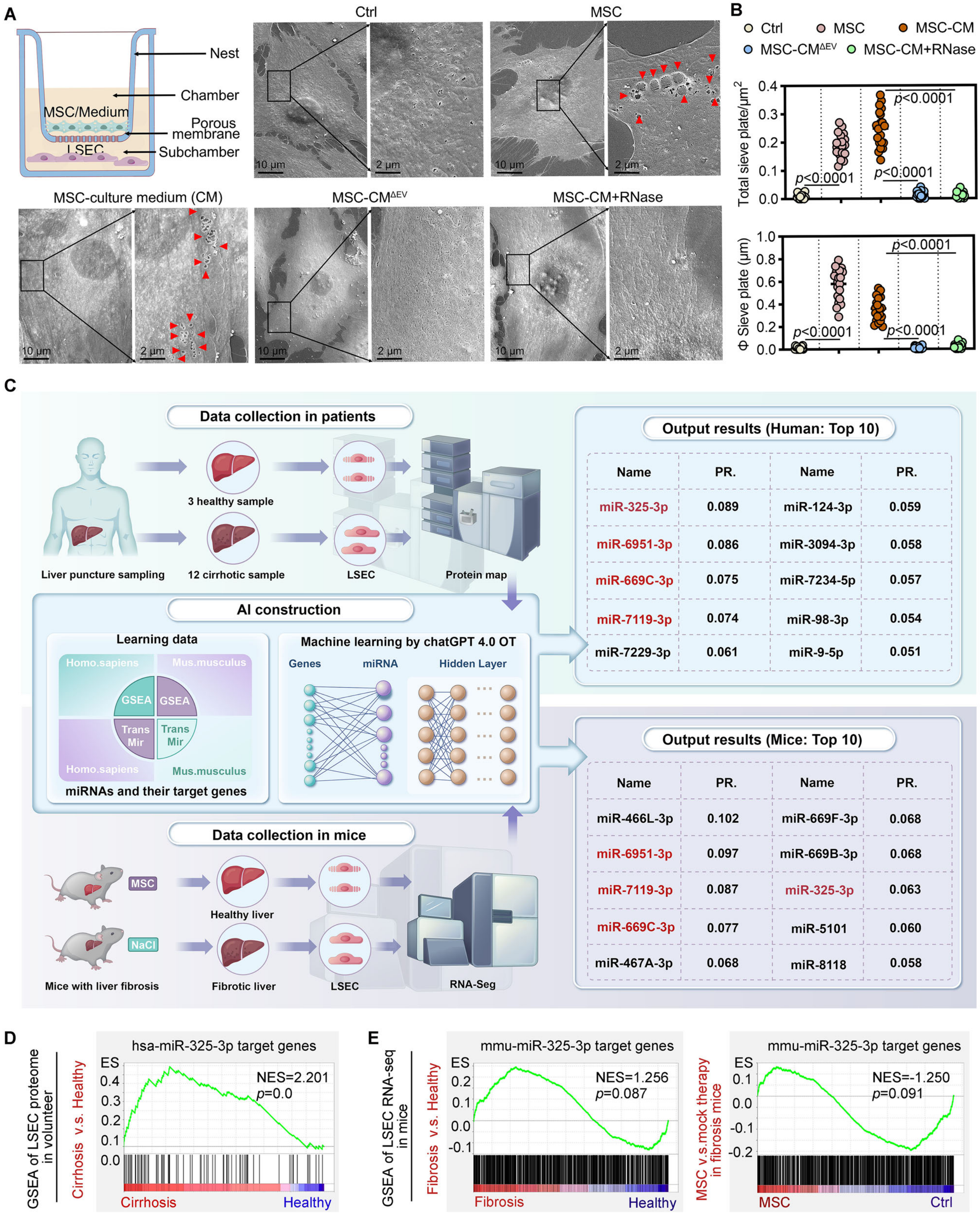

Output results (Human: Top 10)

Name	PR.	Name	PR.
miR-325-3p	0.089	miR-124-3p	0.059
miR-6951-3p	0.086	miR-3094-3p	0.058
miR-669C-3p	0.075	miR-7234-5p	0.057
miR-7119-3p	0.074	miR-98-3p	0.054
miR-7229-3p	0.061	miR-9-5p	0.051

Output results (Mice: Top 10)

Name	PR.	Name	PR.
miR-466L-3p	0.102	miR-669F-3p	0.068
miR-6951-3p	0.097	miR-669B-3p	0.068
miR-7119-3p	0.087	miR-325-3p	0.063
miR-669C-3p	0.077	miR-5101	0.060
miR-467A-3p	0.068	miR-8118	0.058

Fig. 1 | AI-assisted exploration of the reversal of LSEC capillarization by MSCs. **A** LESC cell line was divided into five groups, including LSEC without treatment, co-cultured with MSCs, treated with MSCs culture medium (CM) with/without extracellular vesicles (EV) and RNase, scanning electron microscopy (SEM) was performed 48 hours after incubation. Scale bar 10 μm and 2 μm. A schematic diagram of cell processing was shown in the upper left panel. Red arrows indicate the fenestrae and sieve plates. **B** The quantification of the percentage of sieve plates to total surface area and diameter of sieve plates. *p*-values were calculated by One-way analysis of variance (ANOVA). **C** The potential miRNA utilized by MSC for the reversal of LSEC capillarization was identified through the development of ChatGPT 4.0 oT artificial intelligence (AI) models, which were trained on human and mouse miRNAs as well as their corresponding target genes from GSEA and TargetScan databases. **D**, **E** Gene set enrichment analysis (GSEA) was conducted on hsa/mmu miR-325-3p target genes using both proteomic data (**D**) and RNA-seq data (**E**).

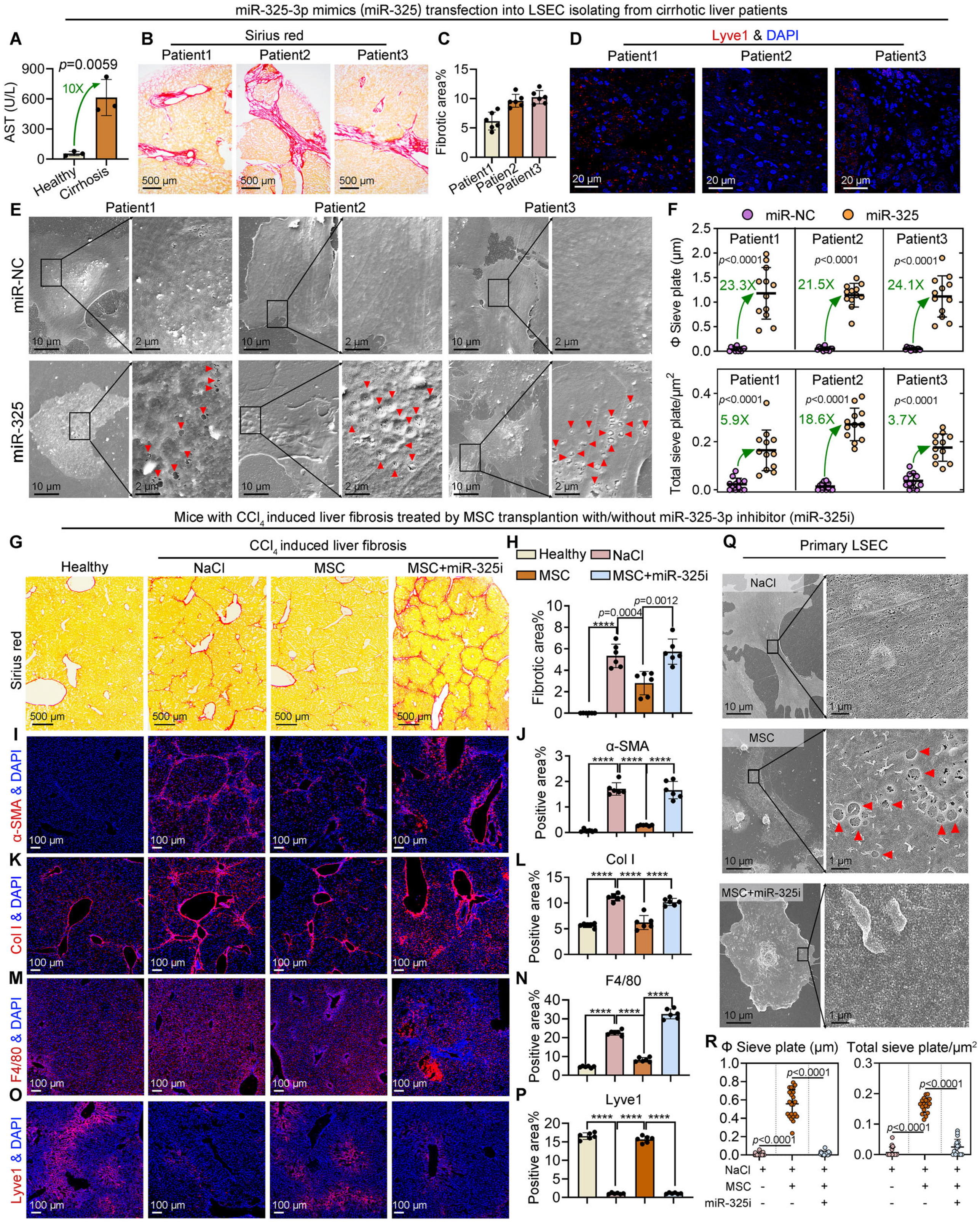

mice treated with NaCl, MSC, or miR-325i-treated MSC. Interestingly, we observed a striking disparity between the almost negligible presence of this miRNA in hepatic fibrosis LSEC compared to its remarkably high abundance in MSC (Supplementary Fig. 2D). However, upon transplantation of MSC, miR-325-3p was also detected in LSEC, suggesting that these cells acquire the miRNA from the transplanted MSC (Supplementary Fig. 2D). These findings collectively demonstrate the pivotal role played by MSC-derived miR-325-3p in reversing LSEC capillarization.

The miR-325-3p targets Ptprm to modulate the cytoskeleton of LSECs, reversing their capillarization

To investigate the underlying mechanism by which miR-325-3p reverses LSEC capillarization, we transfected miR-325-3p mimics into LSEC

Fig. 2 | The LSEC capillarization is reversed by MSC in a miR-325-3p-dependent manner. **A** AST analysis was performed on three healthy and three cirrhotic volunteers. ($n = 3$ independent replicates). **B**, **C** Sirius red staining of three patients' liver sections and the quantification of mature collagen stained by Sirius red (**C**). Scale bar 500 μm. **D** Immunofluorescent staining of Lyve-1 analyzed by Confocal Laser Scanning Microscope (CLSM). Scale bar 20 μm. **E** LESCs isolated from three patients were transfected with miR-325-3p and miR-NC, then SEM was performed 48 h after transfection. Scale bar 10 μm and 2 μm. **F** The quantification of the percentage of sieve plates to total surface area and diametar of sieve plates. **G**, **H** Sirius red staining of liver sections of mice under different treatment conditions and the quantification of mature collagen stained by Sirius red (**H**). ($n = 6$ independent replicates). **I**–**P** Immunofluorescent staining and quantification (**I**) of α-SMA, Col I, F4/80 and Lyve-1. **Q** Phenotypic change of primary LSECs isolated from three different groups were examined by SEM. Scale bar 10 μm and 2 μm. Red arrows indicate the fenestrae and sieve plates. **R** The quantification of the percentage of sieve plates to total surface area and diameter of sieve plates. In (**A**, **C**, **F**, **H**, **J**, **L**, **N**, **P**, **R**), the data are shown as the mean ± SD. *p*-values in (**A**, **F**) were calculated by the unpaired two-tailed Student's t-test; in (**C**, **H**, **J**, **L**, **N**, **P**, **R**) were calculated by one-way analysis of variance (ANOVA). **** $p < 0.0001$.

cell lines. This resulted in a significant downregulation of 448 proteins compared to mock treatment, as measured by iTRAQ (Isobaric tag for relative and absolute quantitation) proteome analysis (Fig. 3A). By intersecting these proteins with the target genes of miR-325-3p, we identified four genes: Madk, Csn2, Ptprm, and Ngly1 (Fig. 3B). Further analysis revealed that only Ptprm showed a statistically significant decrease in expression in response to MSC transplantation in LSEC cells (Fig. 3C), suggesting that Ptprm is a potential target gene of miR-325-3p in reversing LSEC capillarization. Additionally, the expression level of Ptprm in LSECs isolated from patients with liver cirrhosis is significantly higher than that in LSECs from healthy livers (Supplementary Fig. 3A). Similarly, Ptprm expression is elevated in LSECs isolated from CCl_4-treated mice with liver cirrhosis compared to those from control mice with healthy livers (Supplementary Fig. 3B). These findings provide additional evidence supporting the proposed hypotheses. Furthermore, we identified a specific binding site between miR-325-3p and the mRNA 3'UTR of Ptprm (Fig. 3D). Dual luciferase reporter gene assays revealed that overexpression of miR-325-3p significantly attenuated luciferase activity specifically in Ptprm-WT expressing cells, while having no significant impact on cells expressing Ptprm-MUT (Fig. 3E). Western blot analysis further validated that ectopic expression of miR-325-3p markedly reduced protein levels of Ptprm in MSC cells compared to control groups (miRNA negative control or inhibitor negative control), whereas transfection with miRNA inhibitors exerted the opposite effect (Fig. 3F). Notably, to confirm the conserved biofunction of human and mouse miR-325-3p in this study, we demonstrated their ability to down-regulate Ptprm. As illustrated in Supplementary Fig. 3C, consistent with human miR-325-3p, mmu-miR-325-3p significantly reduced Ptprm protein levels in MSC cells compared to control groups (miRNA negative control or inhibitor negative control). Conversely, transfection with their respective inhibitors produced an opposing effect. Furthermore, the transcriptional inhibition of Ptprm by human and mouse miR-325-3p in LSEC was found to be nearly identical, as evidenced by the RT-PCR results (Supplementary Fig. 3D). These findings collectively suggest that the use of human miR-325-3p in this study is well-founded. Additionally, transfecting LSEC cells with small interfering RNA targeting Prprm (si-Ptprm) resulted in a remarkable 71% decrease of the Ptprm mRNA (Supplementary Fig. 3E), which demonstrated comparable efficacy to miR-325-3p in effectively restoring the fenestrations and sieve plate structures of differentiated LSECs (Fig. 3G, H). Collectively, these results establish Ptprm as a direct target gene of miR-325-3p capable of effectively reversing LSEC capillarization.

Receptor protein tyrosine phosphatase mu (PTPμ), which is encoded by the Ptprm gene, has been demonstrated to regulate cytoskeletal organization through modulating the phosphorylation level of p120-catenin[24,25]. This regulatory mechanism plays a critical role in controlling the formation and maintenance of fenestrations and sieve plate structures in liver sinusoidal endothelial cells (LSECs)[26,27]. In line with this, the Gene Ontology (GO) analysis of iTRAQ proteome results comparing LSECs transfected with miR-325-3p mimics (Supplementary Fig. 3F) or control miRNA revealed a significant up-regulation in microtubule binding and filamentous actin binding (Fig. 3I). This finding was further supported by the GSEA results (Fig. 3J and Supplementary Fig. 3G). Consistent with these findings, miR-325-3p effectively reverses LSEC capillarization through modulation of their cytoskeleton, as evidenced by substantial improvements in tubulin and actin protein levels and assembly (Fig. 3K–M). Moreover, the cytoskeletal assembly agonist Bis-T23 and the inhibitor CK666 were employed to further investigate the underlying mechanism. Bis-T23, which stimulates actin-dependent Dynamin oligomerization to promote cytoskeletal assembly[28], exhibited effects similar to those of miR-325-3p in enhancing tubulin and actin levels in LSECs (Supplementary Fig. 3H) and subsequently restoring the fenestrations and sieve plate structures of differentiated LSECs (Supplementary Fig. 3I). In stark contrast, CK666, an inhibitor of cytoskeletal assembly that modulates actin branching and polymerization by inhibiting the activity of the Arp2/3 complex[29], completely abrogated the bioactivity of miR-325-3p on both the enhancement of tubulin/actin protein levels (Supplementary Fig. 3H) and the restoration of the fenestrations and sieve plate structures of differentiated LSECs (Supplementary Fig. 3I). Additionally, si-Ptprm transfection also resulted in the reversal of LSEC capillarization (Fig. 3N) and an increase in microtubule binding and filamentous actin binding (Fig. 3O), as evidenced by RNA-seq data. Collectively, miR-325-3p reverses LSEC capillarization by directly targeting the Ptprm, thereby triggering cytoskeletal reorganization that enhances microtubule and actin filament assembly and ultimately restores fenestrations and sieve plate structures in LSECs. Besides, it is worth noting that co-culture experiments demonstrated that miR-325-3p-transfected LSECs significantly suppress macrophage polarization toward the M1 phenotype (Supplementary Fig. 3J), thereby potentially modulating inflammatory responses and inhibiting the progression of liver fibrosis.

The construction of a spherical nucleic acid (SNAs) incorporating miR-325-3p with targeted internalization into LSECs

To specifically deliver miR-325-3p to liver LSEC during the treatment of liver fibrosis, we initially explored the genetic characteristics of various hepatic cell types through single-cell sequencing analysis in mice with hepatic fibrosis. Through this methodology, we successfully identified 11 distinct cell types, including differentiated liver sinusoidal endothelial cells (Di LSEC) and dedifferentiated liver sinusoidal endothelial cells (De LSEC) (Fig. 4A). The heatmap illustrated the top five genes that were uniquely expressed in each cell type, as depicted in Fig. 4B. Notably, among the genes expressed in dedifferentiated LSECs (De LSEC), Scara3 emerged as an outer membrane protein, which may serve as a promising target for delivery applications[30]. Furthermore, the expression level of Scara3 in dedifferentiated LSEC was significantly higher compared to other cells within the fibrotic liver tissue (Fig. 4C), indicating its promising feasibility as a target for efficient LSEC-specific delivery. Moreover, ELISA was utilized to quantify the levels of Scara3 in liver sinusoidal endothelial cells (LSECs) isolated from fibrotic and healthy liver tissues. The results demonstrated that Scara3 levels were significantly elevated in fibrotic samples compared to those in healthy controls (Supplementary Fig. 4A). Furthermore, within fibrotic liver tissue, Scara3 expression was markedly higher in LSECs than in Kupffer cells (Supplementary Fig. 4B), providing additional evidence for Scara3 as a marker specific to dedifferentiated LSECs. Fortunately, Scara is reputed to possess a remarkable affinity

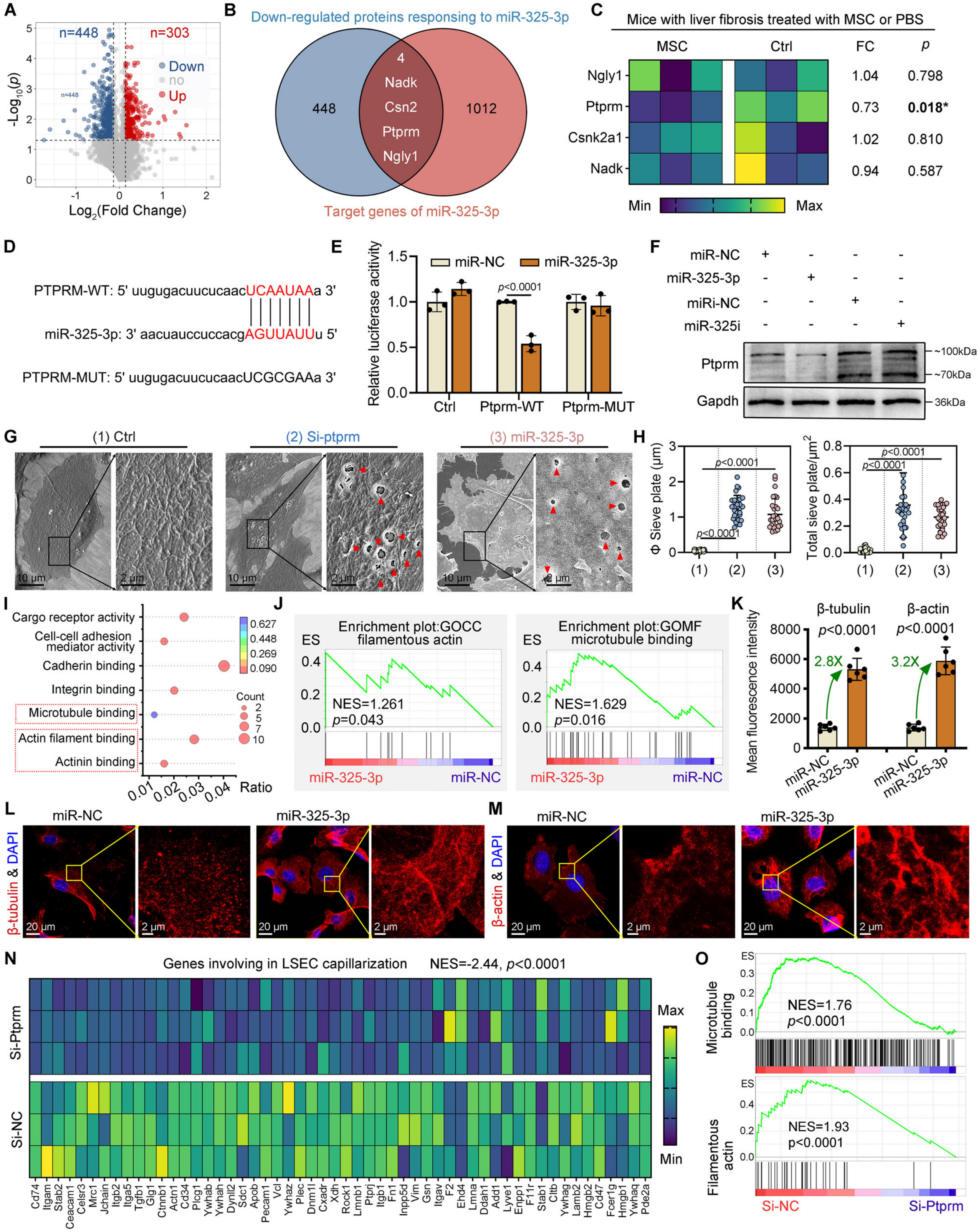

for spherical nucleic acids[17,18], which has served as our inspiration to ingeniously engineer the assembly of miR-325-3p into spheroid polymeric nucleic acid particles with the precise aim of targeting Scara in LSEC. Furthermore, this approach may aid in overcoming yet another pharmaceutical barrier for miRNA - the cellular internalization. The hydrophilic spherical structure, along with the electronegativity of nucleic acids and Scara affinity, can facilitate the internalization of these spheroid polymeric nucleic acids into LSEC cells. The present study employs a mild and biocompatible self-assembly driven by aurophilic interaction to elegantly assemble sulfhydryl and Au(I)-modified miR-325-3p into an enchanting spheroid polyhedron, thus dubbing this assembled miR-325-3p as spherical nucleic acids, SNAs (Fig. 4D). All that remains is to meticulously select the most appropriate size of SNAs for triggering endocytosis.

Fig. 3 | The miR-325-3p targets Ptprm to modulate the cytoskeleton of LSECs, reversing their capillarization. **A** Volcano Plot of differential proteins in LSEC before and after transfection of miR-325. **B** Venn diagram of miR-325-3p target genes related to down-regulated proteins responsing to miR-325-3p in (**A**). **C** The expressions of four genes found in (**B**) in LSECs isolated from CCl_4-induced liver fibrosis before and after MSC treatment. **D** Between Ptprm mRNA 3'UTR and miR-325-3p, the predicted binding sequence is shown in the diagram. **E** To verify the binding relationship between Ptprm mRNA 3'UTR and miR-325-3p, a dual-luciferase reporter gene assay was used. ($n = 3$ independent replicates). **F** Western blot analysis was employed to detect the expression levels of Ptprm in LSECs transfected with miR-325-3p mimics or inhibitors. ($n = 3$ independent replicates). **G** Phenotypic change of LSECs treated in three different methods were examined by SEM. Scale bar 10 μm and 2 μm. Red arrows indicate the fenestrae and sieve plates. **H** The quantification of the percentage of sieve plates to total surface area and diametar of sieve plates. ($n = 6$ independent replicates). **I**, **J** The cell adhesion and microtubule pathways were subjected to gene set enrichment analysis using proteome data obtained from the primary LSECs via LC-MS with a 4D label-free method, comparing miR-325-3p versus miR-NC. ($n = 3$ independent replicates).
K, **M** Immunofluorescent staining of β-tubulin (**L**) and β-actin (**M**) in LSECs incubated with miR-NC and miR-325-3p for 48 h was analyzed by CLSM. Positive signals were quantified via Image J (**K**). ($n = 6$ independent replicates). **N**, **O** Single sample Gene Set Enrichment Analysis (ss-GSEA) were conducted between Si-Ptprm and Si-NC transfected LSECs of LSEC capillarization (N), microtubule binding pathway and filamentous actin pathway (**O**). ($n = 3$ independent replicates). The data are shown as the mean ± SD. p values in (**E**, **H**, **K**) were calculated by one-way analysis of variance (ANOVA).

Then, a series of SNAs with hydrated particle sizes ranging from 13 nm to 102 nm were synthesized. This was achieved by utilizing different concentrations of miR-325-3p with sulfhydryl and Au(I) modification, as well as varying the pH conditions (Supplementary Fig. 4C, E). Subsequently, the cellular internalization of these SNAs into LSEC and macrophage cell line Raw264.7 were assessed through laser scanning confocal microscopy (LSCM), following a 6 h co-incubation period between cells and SNAs. It was observed that SNAs-39nm exhibited the highest uptake by LSECs, while showing relatively low uptake by macrophages (Fig. 4F–I). Furthermore, minimal uptake by Kupffer cells was observed for SNAs-39nm (Supplementary Fig. 4D). Due to its exceptional efficiency and selective uptake into LSECs, SNAs-39nm was henceforth referred to as simply "SNAs" for further exploration purposes. Additionally, X-ray photoelectron spectroscopy was utilized to investigate the chemical properties of these SNAs, revealing the characteristic peaks of monovalent Au and bivalent S (Fig. 4J), thus supporting our design's expected chemical composition (Fig. 4D).

SNAs selectively internalized into LSEC through Scara-mediated clathrin-dependent endocytosis

According to our design, SNAs possess the remarkable ability to recognize Scara on the LSEC surface and internalize themselves into it through this receptor, subsequently releasing miR-325-3p to reverse LSEC capillarization (Fig. 5A). Subsequently, we investigated the internalized model and observed that while lower temperatures hindered the internalization of SNAs into LSECs, ATP incubation enhanced it significantly (Fig. 5B and Supplementary Fig. 5A-C), indicating an active uptake process. Next, GSEA conducted on RNA-seq data from LSECs exposed to SNAs revealed a significantly activated clathrin-dependent endocytosis pathway (Fig. 5C, D). Moreover, treatment with Dynasore, a well-characterized inhibitor of clathrin-dependent endocytosis, led to nearly complete abrogation of SNA internalization in liver sinusoidal endothelial cells (LSECs) (Fig. 5E), thereby providing robust validation for this observation. Most critically, both siRNA-mediated knockdown of Scara3 expression in LSECs and surface neutralization of Scara3 using Anti-Scara3 antibody resulted in marked suppression (~ 88% and ~97%, respectively) of SNA internalization (Fig. 5E). These findings conclusively demonstrate that Scara3 functions as the specific receptor mediating clathrin-dependent endocytosis of SNAs by LSECs. Furthermore, given the significantly higher expression levels of Scara3 in LSECs compared to Kupffer cells (Supplementary Fig. 4B), and considering the intrinsic Scara3-dependent mechanism of SNAs internalization, SNAs exhibited markedly enhanced accumulation in LSECs relative to Kupffer cells (Fig. 4F–I). Besides, since clathrin-dependent endocytosis is frequently associated with the transfer of cargo from the endosome to the lysosome, it is crucial to investigate the ability of miRNA in SNAs to escape degradation within the endosomal-lysosomal pathway. As illustrated in Supplementary Fig. 5D, by employing FITC-conjugated miR-325-3p-labeled fluorescent SNAs, we observed a gradual decrease in the co-localization between green and red fluorescence in early and late endosomes, as well as in lysosomes. This indicates efficient endosomal escape and minimal lysosomal degradation of miR-325-3p.

To further validate the in vivo LSEC targeting, inductively coupled plasma mass spectrometry (ICP-MS) was employed to quantify the ^{197}Au content in each organ following intravenous injection of SNAs into mice with CCl_4-induced liver fibrosis, thereby enabling calculation of the biodistribution of SNAs. As anticipated, both at 2 h and 2 days post-injection, the liver exhibited the highest accumulation of SNAs among the major organs (Fig. 5F). More intriguingly, the fibrotic liver targeting accumulation can be effectively hindered by the Scara neutralizing antibody. Specifically, when administered intravenously at a dosage of 5 mg/kg, Anti-Scara injection 12 hours prior to SNAs injection resulted in an unexpected accumulation in the spleen rather than the liver (Supplementary Fig. 5E), providing further evidence for the Scara-dependent mechanism underlying the fibrotic liver targeting accumulation of SNAs. Moreover, considering that Kupffer cells may reside outside the LSEC due to hepatic sinus structure, it becomes imperative to investigate their predatory uptake of SNAs. Hence, colocalization analysis between SNAs fluorescence and Kupffer cell marker F4/80, as well as LSEC marker Stablin2 fluorescence signal (Fig. 5G), revealed conspicuous colocalization between SNAS and Stablin2 rather than SNAs and F4/80, suggesting that a vast majority of internalized SNAS is localized within LSEC instead of Kupffer cells. These in vivo findings unequivocally demonstrate targeted delivery to LSEC in mice with liver fibrosis.

Additionally, the rapid degradation of miRNA poses a significant challenge for the clinical translation of nucleic acid drugs. Fortunately, SNAs offer a solution to this obstacle by effectively prolonging the half-life period of miR-325-3p to over 30 h in a PBS solution containing 20% serum, whereas naked miR-325-3p exhibited a half-life period of less than an hour (Supplementary Fig. 5F, G). Additionally, in order to further validate the universality of SNAs, we also employed a MicroRNA with a random sequence to fabricate the spherical nucleic acid, which we have designated as SNAs-R. As anticipated, SNAs-R exhibited a similar propensity for fibrotic liver accumulation as SNAs (Supplementary Fig. 5H), while demonstrating exceptional resistance against degradation (Supplementary Fig. 5I, J). These findings strongly suggest that SNAs represent an all-encompassing technology capable of selectively internalizing into LSEC and safeguarding MicroRNA from degradation.

SNAs effectively reversed the capillarization of LSEC and demonstrated remarkable therapeutic efficacy in various mouse models of liver fibrosis

The successful targeting of SNAs in mice with liver fibrosis prompted us to investigate its efficacy in vivo. The initial mouse model selected to assess the potential of SNAs was CCl_4-induced liver fibrosis, which replicates the pathogenesis resulting from oxidative stress associated with unhealthy habits, aging, or acute and chronic liver injuries (Fig. 6A)[31,32]. After successful modeling, a total of 300 μL of SNAS

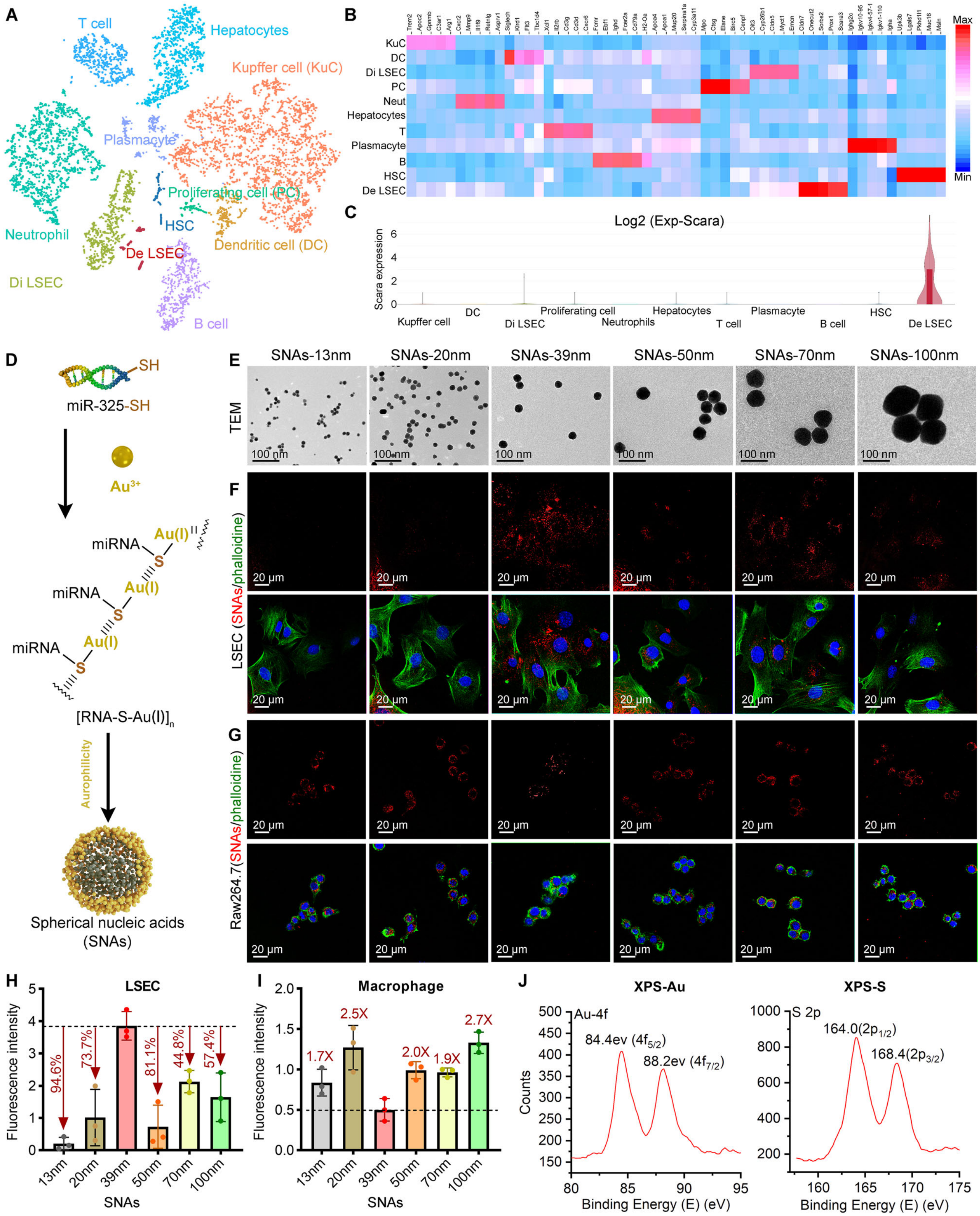

Fig. 4 | The construction of the spherical nucleic acids (SNAs) incorporating miR-325-3p with targeted internalization into LSECs. A t-Distributed Stochastic Neighbor Embedding (t-SNE) plots of broad cell types within the liver tissue in CCl_4-induced liver fibrosis mice (*n* = 3 independent replicates). **B** The heatmap revealed the top five genes that were uniquely expressed in each hepatic cell type. **C** The expression level of Scara in each hepatic cell type. **D** The diagram of synthesis procedure for the spherical nucleic acids (SNAs). **E** TEM images of SNAs with hydrodynamic diameters ranging from 13 nm to 102 nm. **F**, **G** Laser Scanning Confocal Microscope (LSCM) images depicting the cellular uptake of different SNAs by LSEC (**F**) and macrophages (**G**). SNAs were labeled in red with Cy3, and cell profiles were highlighted in green using FITC-labeled phalloidine. **H**, **I** Fluorescence intensity analysis of internalized SNAs in LSEC (**H**) and macrophages (**I**). *n* = 3 independent replicates in each group. The data are shown as the mean ± SD. **J** The X-ray photoelectron spectroscopy reveals the electron spectra of SNAs with a size of 39 nm, specifically in its Au-4f and S-2p orbitals.

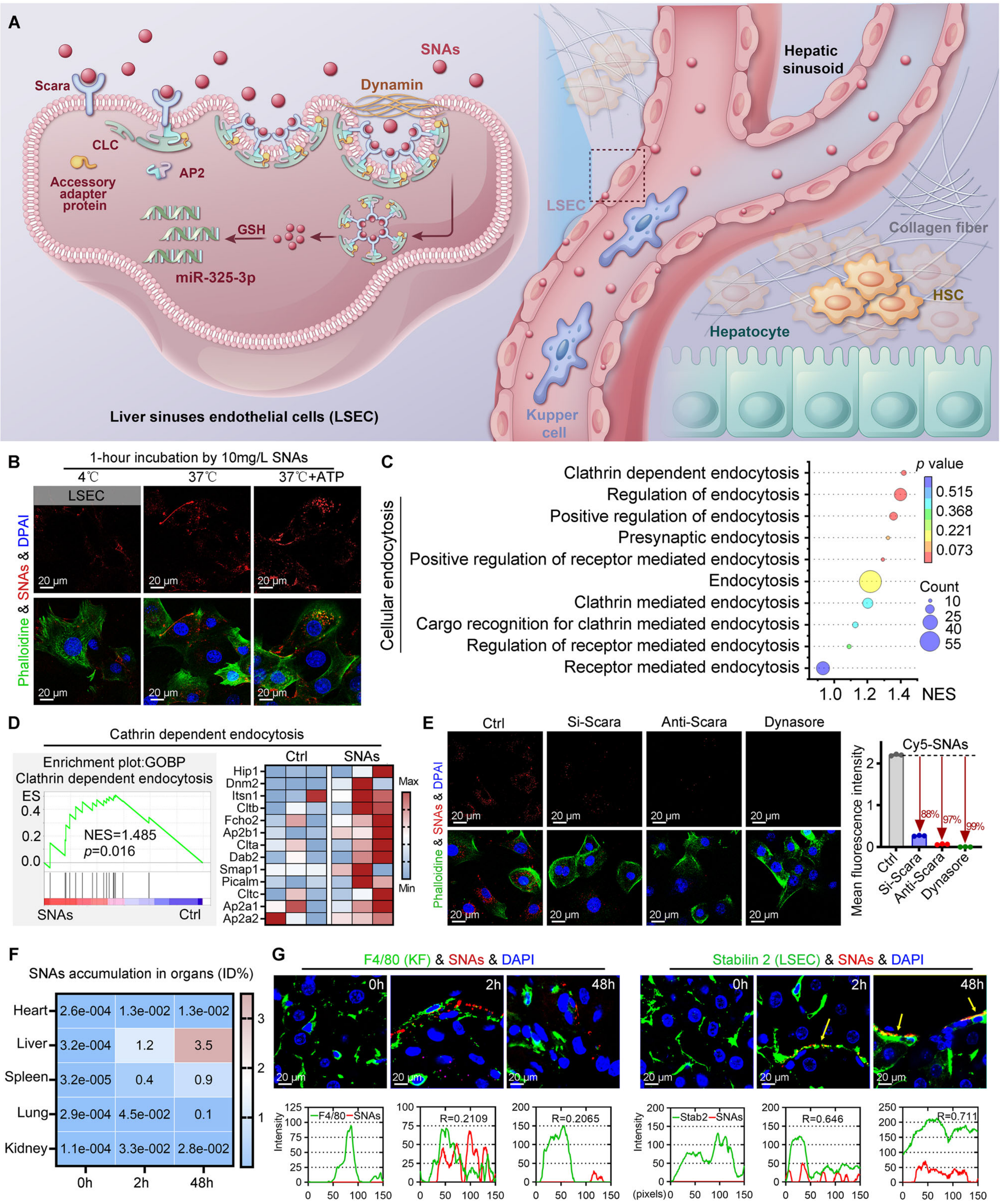

Fig. 5 | The cellular internalization pathway and in vivo biodistribution of SNAs. **A** The schematic diagram of LSEC endocytosis and liver homeostasis. **B** The LSCM images illustrate the cellular uptake of SNAs into LSEC after a 1-hour incubation at 4 °C, 37 °C, and 37 °C with ATP. **C** GSEA analysis was performed to investigate the impact of SNAs treatment on the cellular endocytosis pathway, using proteome results obtained from LSECs treated with SNAs and mock-treated controls. (*n* = 3 independent replicates, means ± SD). **D** GSEA analysis and protein levels of clathrin-dependent endocytosis of SNAs-treated and mock-treated LSECs. **E** The LSCM images and fluorescence intensity analysis illustrate the cellular uptake of SNAs into LSEC after a 12 h pro-incubation with si-Scara, Anti-Scare or Dynasore. *n* = 3 independent replicates in each group. The data are shown as the mean ± SD. **F** Accumulation of SNAs in organs and tissues were reflected by the concentration of Au detected by ICP-MS in CCl_4-induced fibrosis mice. Serial euthanasia was carried out at different time points (2 h and 48 h) after systemic injection. (*n* = 3 independent replicates, means ± SD). **G** An immunofluorescence analysis of F4/80 (left) and Stabilin 2 (right) co-localized with Cy3-SNAs was performed on liver tissues of fibrotic mice at 2 h and 48 h following tail vein injection of Cy3-SNAs. Double positive signals were quantified and showed in lower panel. (*n* = 3 independent replicates, means ± SD).

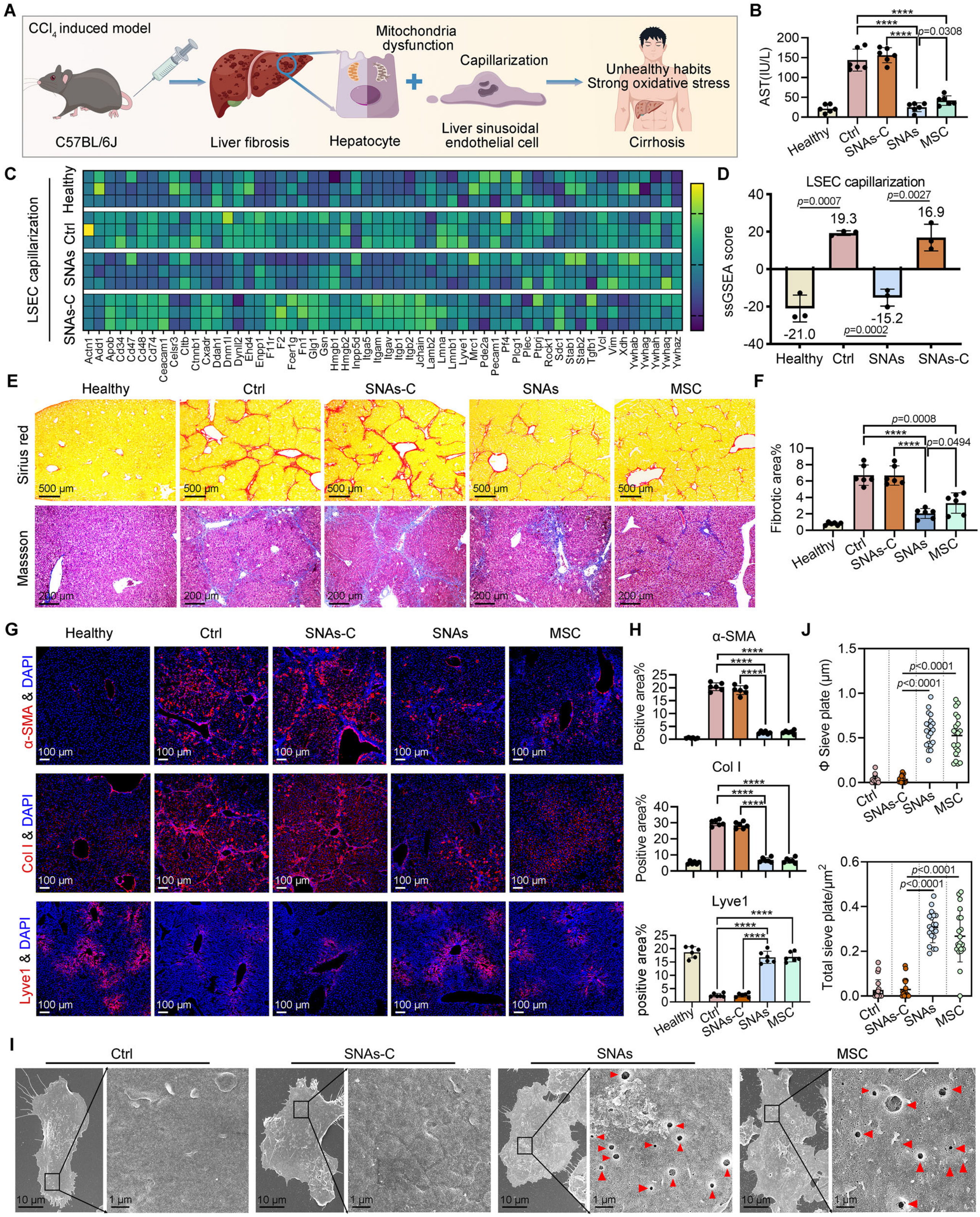

containing 0.3OD miR-325-3p were intravenously administered. As negative controls, a control SNAS consisting of a random sequence of miR-325-3p (SNAs-C) and an equal volume of normal saline (Ctrl) were employed. Furthermore, to establish a positive control, tail intravenous injection of 2×10^5 MSCs was performed, while six healthy mice served as block controls. It is noteworthy that all administrations were single-dose therapies. After 10 days of administration, all mice were euthanized to assess liver fibrosis. As depicted in Supplementary Fig. 6A, both SNAs and MSCs significantly reduced the Ptprm level, nearly restoring it to that observed in healthy liver tissue. The liver function index AST in both SNAs and MSC treated sick mice returned to normal levels, similar to healthy mice (Fig. 6B). In contrast, SNAs-C and mock treated sick mice showed significantly higher AST levels compared to the other three groups (Fig. 6B). Subsequent RNA-seq

Fig. 6 | SNAs effectively reversed the capillarization of LSEC and demonstrated remarkable therapeutic efficacy in CCl_4-induced liver fibrotic model. A The schematic diagram of CCl_4-induced liver fibrosis in mice and corresponding clinical cirrhosis types. **B** An analysis of AST was performed on five different serum samples, including samples from healthy mice and fibrotic mice that were treated with saline (Ctrl), SNAs-C, SNAs, and MSC. **C**, **D** Single sample Gene Set Enrichment Analysis (ss-GSEA) were conducted on LSECs isolated from healthy mice and fibrotic mice that were treated with saline, SNAs-C and SNAs for LSEC capillarization. **E**, **F** Sirius red and masson staining of liver sections of mice under different treatment conditions and the quantification of mature collagen stained by Sirius red (**F**). **G**, **H** Immunofluorescent staining and quantification (**H**) of α-SMA, Col I and Lyve-1. **I** Phenotypic change of primary LSECs isolated from four different groups were examined by SEM. Scale bar 10 μm and 2 μm. Red arrows indicate the fenestrae and sieve plates. **J** The quantification of the percentage of sieve plates to total surface area and diametar of sieve plates. The data are shown as the mean ± SD ($n = 3$ for 4D label-free analysis and $n = 6$ for CCl_4-induced mice model and treatment). p values in (**B**, **F**, **H**, **J**) were calculated by One-way analysis of variance (ANOVA). $^{****}p < 0.0001$.

results of LSEC capillarization-related genes (Fig. 6C) from isolated LSECs and their signal simple GSEA analysis (ssGSEA in Fig. 6D) revealed that SNAs effectively reversed LSEC capillarization at the transcriptional level, unlike SNASC. Additionally, the GSEA analysis of data obtained from isolated LSECs in SNAS-treated mice compared to mock-treated mice also unveiled an up-regulation of filamentous actin and microtubule binding, aligning perfectly with the aforementioned mechanism of miR-325-3p (Supplementary Fig. 6B). Importantly, the gold standard assessment for liver fibrosis using collagen staining by Sirius red and Masson demonstrated that SNAs significantly reduced the fibrotic area in the liver from approximately 7% to less than 3%, which was more effective than MSC treatment at 3.5% (Fig. 6E, F). Consistent with these findings, both SNAs and MSC statistically decreased the up-regulated levels of active HSC marker α-SMA and Col I in the fibrotic liver while increasing expression of differentiated cell LSEC marker Lyve-1 (Fig. 6G, H). Furthermore, SEM images of isolated LSECs from these sick mice further supported these results by showing that both SNAs and MSC not only increased sieve plate diameter but also enhanced sieve plate quantity (Fig. 6I, J). This demonstrates the alternative efficacy of MSC treatment with SNAs in effectively restoring fenestrations and sieve plate structures in differentiated LSECs.

Additionally, subsequent to the administration, an exploration was conducted on hematotoxicity and organ toxicity. As evidenced by the routine blood test (Supplementary Fig. 7A), renal function assessment (Supplementary Fig. 7B), as well as histopathological examination of the heart, spleen, lung, and kidney sections (Supplementary Fig. 7C), no indications of hematotoxicity or organ toxicity were observed in mice treated with both SNAs and SNAs-C. Moreover, transcriptomic analyses of spleen tissues following SNA administration revealed no significant changes in immune cell populations or activation states (Supplementary Fig. 8). Collectively, these findings conclusively demonstrate that SNAs have the capacity to reverse LSEA capillarization and effectively treat liver fibrosis while maintaining an excellent biosafety profile.

The subsequent step entailed challenging the efficacy of SNAs in a murine model of TAA-induced liver fibrosis, which serves as an exemplary model for drug-induced hepatocyte demise (Fig. 7A)[33,34]. Following the same therapeutic administration protocol as in CCl_4-induced liver fibrosis, SNAs significantly decreased the Ptprm level, nearly restoring it to that of healthy liver tissue (Supplementary Fig. 9A). Meanwhile, SNAs effectively ameliorated the elevated levels of AST in TAA-induced liver fibrosis mice and significantly reduced the extent of fibrotic area in comparison to both mock and SNAs-C treated livers (Fig. 7B–D). Consistent with these findings, SNAs exhibited a statistically significant decrease in the up-regulated expression levels of α-SMA, an active HSC marker (Fig. 7E, F), as well as F4/80, an active Kupffer cell marker (Supplementary Fig. 9B) within the fibrotic liver. Additionally, it also rectified the down-regulated expression levels of Lyve1, a differentiated cell LSEC marker (Fig. 7E, F). Furthermore, SEM images of isolated LSECs further corroborated these results by demonstrating that SNAS not only increased sieve plate diameter but also enhanced sieve plate quantity (Fig. 7G, H). These outcomes unequivocally establish that SNAs possesses the ability to reverse LSEA capillarization and thus effectively treats TAA-induced liver fibrosis.

The next challenge for SNAs arose in the fibrosis mice model induced by cholestasis, which was established through surgical bile duct ligation (BDL) (Fig. 7I)[35,36]. As anticipated, SNAs significantly decreased the Ptprm level, nearly restoring it to that of healthy liver tissue (Supplementary Fig. 9C). Moreover, SNAs effectively ameliorated the BDL-induced up-regulation of AST (Fig. 7J), while significantly reducing the fibrotic area to a state comparable to that of healthy mice (Fig. 7K, L). Additionally, SNAs demonstrated a significant decrease in the elevated levels of active HSC marker α-SMA (Fig. 7M, N) and ColI (Supplementary Fig. 9D) in the fibrotic liver, accompanied by an increase in expression of differentiated cell LSEC marker Lyve-1 (Fig. 7M, N). Furthermore, SEM images of isolated LSECs revealed that SNAs restored sieve plate diameter and quantity to normal levels observed in healthy individuals (Fig. 7O, P). Collectively, these findings illustrate that SNAs possesses the ability to reverse LSEA capillarization and effectively treat BDL-induced liver fibrosis. Notably, it is worth mentioning that SNASC exhibited negligible efficacy across all three liver fibrosis models, highlighting miR-325-3p as solely responsible for the potency observed with SNAs.

Discussion

The clinical challenge posed by liver fibrosis, characterized by excessive accumulation of extracellular matrix, remains significant to this day[37]. The therapeutic potential of LSECs in reversing fibrosis has garnered considerable attention and interest[38,39]. Traditional approaches, such as MSC transplantation, have demonstrated efficacy in reversing LSEC capillarization and alleviating fibrosis[6,8]. However, MSC therapy faces limitations including safety concerns such as tumorigenicity, immune rejection, ethical issues, and high costs[15,16]. This study not only unveiled the underlying mechanism of MSC-induced reversal of LSEC capillarization by intricately secreting miR-325-3p to modulate the cytoskeleton of LSECs, thereby reinstating their fenestrations and sieve plate structures and returning them to their differentiated state, but also introduced a bionic Spherical nucleic acid (SNAs) specifically engineered to selectively target LSECs while harnessing miR-325-3p to regulate the cytoskeleton and restore LSEC functionality. Consequently, this approach addresses the limitations associated with MSC therapy and offers a safer and more effective alternative.

Replacing MSCs with SNAs for the treatment of liver fibrosis offers several advantages. Firstly, SNAs specifically targets LSECs, ensuring precise delivery of therapeutic agents and minimizing off-target effects while enhancing efficacy. The targeted delivery of SNAs is facilitated by the overexpression of Scara in hepatic fibrotic LSECs, allowing selective infiltration and therapeutic action. This targeted mechanism highlights the superiority of SNAs over MSCs, providing a more controlled, efficient, and safer therapeutic option for liver fibrosis. Secondly, unlike MSCs, SNAs avoids potential issues related to cell sourcing and ethical dilemmas as it does not involve live cell transplantation[14]. Moreover and most importantly, preclinical models have demonstrated that 0.3 OD miR-325-3p-containing SNAs exhibits superior performance by effectively reversing LSEC capillarization and reducing fibrosis markers comparable or even more significantly than MSCs.

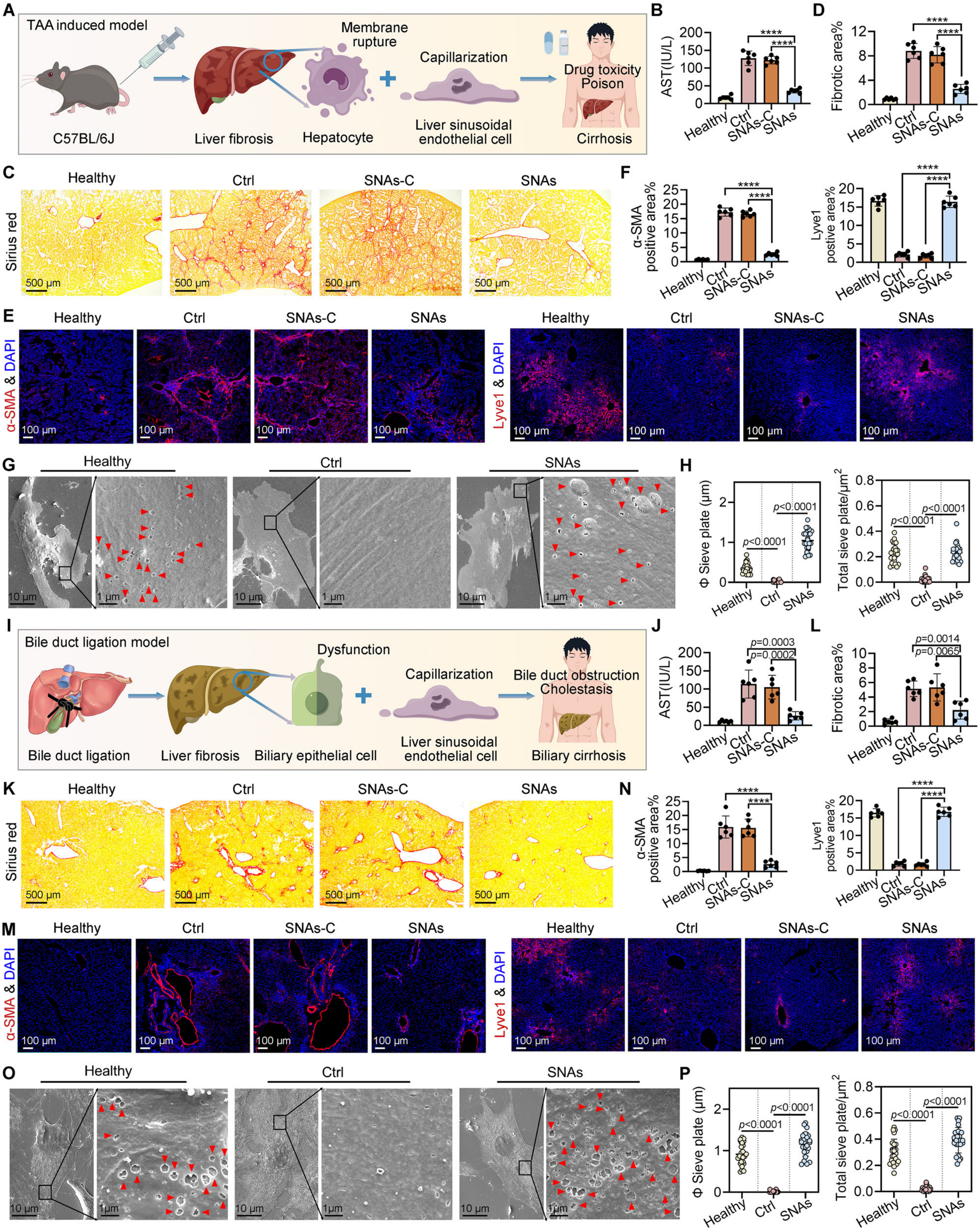

In summary, our study highlights the immense potential of SNAs in the treatment of liver fibrosis by specifically targeting LSECs and reversing their capillarization. Through innovative design and precise delivery mechanisms, SNAs effectively restored the structure and functionality of LSECs, leading to a reduction in fibrosis and an improvement in liver function across multiple preclinical models. The discovery of miR-325-3p's role in reversing LSEC capillarization through Ptprm targeting further enhances our understanding of the therapeutic mechanisms involved at a molecular level, thereby advancing our knowledge on fibrosis treatment. These findings position SNAs as a promising alternative to MSC therapy, instilling hope for patients suffering from chronic liver diseases. Furthermore, the remarkable advancement of SNAs strongly suggests that they embody a universal technique capable of selectively internalizing into LSECs

Fig. 7 | SNAs effectively reversed the capillarization of LSEC and demonstrated remarkable therapeutic efficacy in TAA-induced liver fibrotic and BDL models. **A** The schematic diagram of TAA-induced liver fibrosis in mice and corresponding clinical cirrhosis types. **B** AST levels in four different samples of serum, including samples from healthy mice and fibrotic mice that were treated with saline (Ctrl), SNAs-C and SNAs. **C**, **D** Sirius red staining of four liver sections and the quantification of mature collagen stained by Sirius red (**D**). **E**, **F** Immunofluorescent staining and quantification (**F**) of α-SMA and Lyve-1. **G** Phenotypic change of primary LSECs isolated from three different groups were examined by SEM. Scale bar 10 μm and 2 μm. Red arrows indicate the fenestrae and sieve plates. **H** The quantification of the percentage of sieve plates to total surface area and diametar of sieve plates. **I** The schematic diagram of bile duct ligation model and corresponding clinical biliary cirrhosis. (**J**) AST levels in four different samples of serum, including samples from healthy mice and fibrotic mice that were treated with saline, SNAs-C and SNAs. **K**, **L** Sirius red staining of four liver sections and the quantification of mature collagen stained by Sirius red (**D**). **M**, **N** Immunofluorescent staining and quantification (**N**) of α-SMA and Lyve-1. **O** Phenotypic change of primary LSECs isolated from three different groups were examined by SEM. Scale bar 10 μm and 2 μm. Red arrows indicate the fenestrae and sieve plates. **P** The quantification of the percentage of sieve plates to total surface area and diametar of sieve plates. The data are shown as the mean ± SD ($n = 6$ for TAA-induced mice model and treatment and $n = 4$ for BDL model and treatment). *p*-values in (**B**, **D**, **F**, **H**, **J**, **L**, **N**, **P**) were calculated One-way analysis of variance (ANOVA). $^{****}p < 0.0001$.

and safeguarding MicroRNA from degradation, thereby paving the way for targeted and highly effective nucleic acid drug therapy specifically tailored to LSECs.

Methods

Animal models and therapies

Three kinds of liver fibrosis animal models were constructed in our study, including carbon tetrachloride (CCl_4), thioacetamide (TAA), and bile duct ligation (BDL). All mice were sourced from the Laboratory Animal Center of Xi'an Jiaotong University (license number: SYXK 2023-004). They were given standard rodent feed and maintained under specific pathogen-free conditions with a regulated light/dark cycle. All procedures and handling of the animals were overseen by the Animal Care Committee of Xi'an Jiaotong University, and the experimental protocols received full approval (No. 20221507).

CCl_4 induced liver fibrosis model. 1 µl/g CCl_4 (CCl_4/sunflower oil: 20%) was intraperitoneally injected to 10-week-old male C57BL/6 mice twice a week for 6.5 weeks. At week 5, mice were given MSC (2×10^5 cells per mouse), SNAs-C (300 µl per mouse) and SNAs (300 µl/0.3 OD miR-325 per mouse) after which routine CCl_4 administration was continued (6 per group). Following 10 days of administration, blood samples were collected for biochemical analysis, and serum was separated. The whole liver and other organs were harvested for further analysis.

TAA induced liver fibrosis model. 10-week-old male C57BL/6 mice were divided into 4 experimental groups, including healthy, Ctrl (TAA), SNAs-C and SNAs (4 per group). Mice models received 200 mg/L TAA in the drinking water for 5 months. At month 4.5, the TAA-induced mice models were treated with SNAs-C or SNAs (300 µl). On day 10 after administration, blood samples and organs were collected.

BDL induced acute liver fibrosis model. Induced acute hepatic fibrosis was achieved by ligating the extrahepatic common bile duct of C57BL/6 mice (4 per group). For a clear view of the hepatic hilum, the ventral side of the liver was raised after the abdominal midline incision. Carefully separate the common bile duct from the hepatic artery and collateral portal vein with ophthalmic tweezers. Then, suture around the common bile duct and fix it with surgical knot. 7 days after BDL operation, mice were intravenously injected with SNAs-C or SNAs (300 µl). On day 7 after administration, blood samples and organs were collected.

Artificial intelligence

An artificial intelligence (AI) model was developed to discern the active miRNA by collaboratively analyzing multiple omics data. Leveraging ChatGPT 4.0, this AI model underwent training through machine learning using human and mouse miRNAs along with their corresponding target genes from GSEA and TargetScan databases. Subsequently, the RNA-seq results obtained from LSECs isolated from mice with CCl_4-induced liver fibrosis, either treated with MSC or mock-treated, were inputted into this AI model to discern the active miRNA responsible for these differentially expressed genes. Similarly, the proteomics results derived from LSECs isolated from 3 healthy donors and 12 patients with cirrhosis were also incorporated into this AI model. By performing these two independent operations, the AI model respectively identified the Top 10 miRNAs most likely responsible for these differences.

Synthesis and characterization of spherical nucleic acid (SNA)

Synthesis: 2 OD sulfhydryl-modified miR-325-3p (hereinafter miR-325) was completely dissolved in 5 mL HEPES buffer (50 nM, pH 7.0) and stirred at 50 °C, 30 g for 10 min. By adding 500 µL of 10 mM $HAuCl_4$ (Aladdin Chemicals), SNAs (39 nm) was successfully synthesized by stirring the solution for approximately 10 minutes until it turned reddish-purple. The same method was used to synthesize control particles, named SNAs-C, but without miR-325. In the process of synthesizing SNA particles, sodium citrate and chloroauric acid can be adjusted to produce particles of various sizes, e.g., particle sizes of 13 nm, 21 nm, 51 nm, 70 nm, and 102 nm, depending on the ratio of 2:1, 1:1, 1:2, 1:4, and 1:8.

Characterization of SNAs: The morphology and lattice structure were examined using high-resolution transmission electron microscopy (Thermo Fisher Sciences, Talos L 120 C G2, USA). Hydrodynamic size distribution was determined via dynamic light scattering (DLS) measurements using a Malvern Zetasizer Nano ZS system (concentration: 1 mg/mL in PBS, volume: 1 mL). To measure the Zeta potential, nanoparticles (1 mg/mL, 1 mL) were incubated in PBS at various pH levels for 30 min at 37 °C and subsequently analyzed using dynamic light scattering. Resistance to degradation of miR-325 and SNAs were compared at 37 °C in 20% FBS, and nucleic acid degradation was detected by agarose gel electrophoresis.

Isolation of primary LSECs from mice models and human specimens

After anticoagulation, anesthesia and vascular perfusion, the liver tissues were removed and cut into small slices, and digested at 37 °C for 1.5 h with 0.5 mg/ml Liberase™ (Roche, 05401127001) prepared in DMEM containing 3% (v/v) fetal bovine serum (FBS) and 250 U/ml DNase I. Tissue fragments were resuspended and mixed intermittently during the enzyme incubation. The tissue suspension was centrifuged at 5 g for 5 min at 4 °C. After centrifugation was continued at 300 g for 10 min, the supernatant was separated from the digestion medium and the LSECs were found in the precipitate. Finally, the precipitate was sorted using the MACS $CD11b^+$ magnetic bead system and the remaining cells which failed to bind to the magnetic beads were used for subsequent culture and analysis.

Reporting summary

Additional details regarding the research design are provided in the Nature Portfolio Reporting Summary associated with this article.

Data availability

The raw sequence data reported in Fig. 4 have been deposited in the Genome Sequence Archive (Genomics, Proteomics & Bioinformatics

2021) in National Genomics Data Center (Nucleic Acids Res 2022), China National Center for Bioinformation / Beijing Institute of Genomics, Chinese Academy of Sciences (GSA: CRA025169) that are publicly accessible at https://ngdc.cncb.ac.cn/gsa. Source data is available for Figs. 1B, 2A, C, F, H, J, L, N, P, R, 3E, H, K, 4H–J, 5E–G, 6B, D, F, H, J, 7B, D, F, H, J, L, N, and P in the associated source data file. Source data are provided with this paper.

References

1. Malarkey, D. E., Johnson, K., Ryan, L., Boorman, G. & Maronpot, R. R. New Insights into Functional Aspects of Liver Morphology. *Toxicol. Pathol.* **33**, 27–34 (2005).
2. DeLeve, L. D. in Seminars in liver disease, Vol. 27 390-400 (© Thieme Medical Publishers, 2007).
3. Shetty, S., Lalor, P. F. & Adams, D. H. Liver sinusoidal endothelial cells—gatekeepers of hepatic immunity. *Nat. Rev. Gastroenterol. Hepatol.* **15**, 555–567 (2018).
4. Ribera, J. et al. A small population of liver endothelial cells undergoes endothelial-to-mesenchymal transition in response to chronic liver injury. *Am. J. Physiol.-Gastrointest. Liver Physiol.* **313**, G492–G504 (2017).
5. Zhao, Y. L., Zhu, R. T. & Sun, Y. L. Epithelial-mesenchymal transition in liver fibrosis (Review). *Biomed. Rep.* **4**, 269–274 (2016).
6. Hammoutene, A. & Rautou, P.-E. Role of liver sinusoidal endothelial cells in non-alcoholic fatty liver disease. *J. Hepatol.* **70**, 1278–1291 (2019).
7. DeLeve, L. D. Liver sinusoidal endothelial cells in hepatic fibrosis. *Hepatology* **61**, 1740–1746 (2015).
8. Cao, Y., Ji, C. & Lu, L. Mesenchymal stem cell therapy for liver fibrosis/cirrhosis. *Ann. Transl. Med.* **8**, 562 (2020).
9. Yin, F., Wang, W. Y. & Jiang, W. H. Human umbilical cord mesenchymal stem cells ameliorate liver fibrosis in vitro and in vivo: From biological characteristics to therapeutic mechanisms. *World J. Stem Cells* **11**, 548–564 (2019).
10. Zhang, L. et al. Stem cell therapy in liver regeneration: Focus on mesenchymal stem cells and induced pluripotent stem cells. *Pharmacol. Therapeutics* **232**, 108004 (2022).
11. Duncan, A. W., Dorrell, C. & Grompe, M. Stem Cells and Liver Regeneration. *Gastroenterology* **137**, 466–481 (2009).
12. Levičar, N. et al. in Bone Marrow-Derived Progenitors. (eds. K. Kauser & A.-M. Zeiher) 243-262 (Springer Berlin Heidelberg, Berlin, Heidelberg; 2007).
13. Park, S. J. et al. Hepatic progenitor cell activation through the interaction of mesenchymal stem cells and liver sinusoidal endothelial cells. *J. Hepatol.* **78**, S442 (2023).
14. Haldar, D., Henderson, N. C., Hirschfield, G. & Newsome, P. N. Mesenchymal stromal cells and liver fibrosis: a complicated relationship. *FASEB J.* **30**, 3905–3928 (2016).
15. Trounson, A. & McDonald, C. Stem cell therapies in clinical trials: progress and challenges. *cell stem cell* **17**, 11–22 (2015).
16. Christiansen, J. R. & Kirkeby, A. Clinical translation of pluripotent stem cell-based therapies: successes and challenges. *Development* **151**, 202067 (2024).
17. Distler, M. E. et al. DNA Dendrons as Agents for Intracellular Delivery. *J. Am. Chem. Soc.* **143**, 13513–13518 (2021).
18. Zhu, Y., Zhu, L., Wang, X. & Jin, H. RNA-based therapeutics: an overview and prospectus. *Cell Death Dis.* **13**, 644 (2022).
19. Zhong, Y., Hu, X. & Liu, J. PGE2 Overexpressing Human Embryonic Stem Cell Derived Mesenchymal Stromal Cell Relieves Liver Fibrosis in an Immuno-suppressive Manner. *Stem Cell Rev. Rep.* **20**, 1667–1669 (2024).
20. Zhang, J. et al. Engineered EVs from LncEEF1G - overexpressing MSCs promote fibrotic liver regeneration by upregulating HGF release from hepatic stellate cells. *Exp. Mol. Med.* **57**, 584–600 (2025).
21. Hu, D., Lai, J., Chen, Q. & Bai, L. New advances of NG2-expressing cell subset in marrow mesenchymal stem cells as novel therapeutic tools for liver fibrosis/cirrhosis. *Stem Cell Res. Ther.* **15**, 199 (2024).
22. Mincheva, G., Moreno-Manzano, V., Felipo, V. & Llansola, M. Extracellular vesicles from mesenchymal stem cells improve liver injury in rats with mild liver damage. Underlying mechanisms and role of TGFβ. *Life Sci.* **364**, 123429 (2025).
23. Liang, Y. et al. Human liver derived mesenchymal stromal cells ameliorate murine ischemia-induced inflammation through macrophage polarization. *Front. Immunol.* **15**, 1448092 (2024).
24. Brady-Kalnay, S. M., Rimm, D. L. & Tonks, N. K. Receptor protein tyrosine phosphatase PTPmu associates with cadherins and catenins in vivo. *J. Cell Biol.* **130**, 977–986 (1995).
25. Hellberg, C. B., Burden-Gulley, S. M., Pietz, G. E. & Brady-Kalnay, S. M. Expression of the Receptor Protein-tyrosine Phosphatase, PTPμ, Restores E-cadherin-dependent Adhesion in Human Prostate Carcinoma Cells. *J. Biol. Chem.* **277**, 11165–11173 (2002).
26. Cogger, V. C. et al. Three-dimensional structured illumination microscopy of liver sinusoidal endothelial cell fenestrations. *J. Struct. Biol.* **171**, 382–388 (2010).
27. Zapotoczny, B. et al. Tracking fenestrae dynamics in live murine liver sinusoidal endothelial cells. *Hepatology* **69**, 876–888 (2019).
28. Sever, S. & Schiffer, M. Actin dynamics at focal adhesions: a common endpoint and putative therapeutic target for proteinuric kidney diseases. *Kidney Int.* **93**, 1298–1307 (2018).
29. Hetrick, B., Han, MinS., Helgeson, LukeA. & Nolen, BradJ. Small Molecules CK-666 and CK-869 Inhibit Actin-Related Protein 2/3 Complex by Blocking an Activating Conformational Change. *Chem. Biol.* **20**, 701–712 (2013).
30. Ezzat, K. et al. Scavenger receptor-mediated uptake of cell-penetrating peptide nanocomplexes with oligonucleotides. *FASEB J.* **26**, 1172–1180 (2012).
31. Dong, S. et al. Mechanisms of CCl_4-induced liver fibrosis with combined transcriptomic and proteomic analysis. *J. toxicological Sci.* **41**, 561–572 (2016).
32. Hayashi, S. et al. Fucoidan partly prevents CCl_4-induced liver fibrosis. *Eur. J. Pharmacol.* **580**, 380–384 (2008).
33. Yang, M.-C., Chang, C.-P. & Lei, H.-Y. Induction of liver fibrosis in a murine hepatoma model by thioacetamide is associated with enhanced tumor growth and suppressed antitumor immunity. *Lab. Investig.* **90**, 1782–1793 (2010).
34. Hsieh, C.-C., Fang, H.-L. & Lina, W.-C. Inhibitory effect of Solanum nigrum on thioacetamide-induced liver fibrosis in mice. *J. Ethnopharmacol.* **119**, 117–121 (2008).
35. Au Tag, C. G. et al. Bile Duct Ligation in Mice: Induction of Inflammatory Liver Injury and Fibrosis by Obstructive Cholestasis. *JoVE.* **96**, e52438 (2015).
36. Xia, J.-L., Dai, C., Michalopoulos, G. K. & Liu, Y. Hepatocyte Growth Factor Attenuates Liver Fibrosis Induced by Bile Duct Ligation. *Am. J. Pathol.* **168**, 1500–1512 (2006).
37. Kisseleva, T. & Brenner, D. Molecular and cellular mechanisms of liver fibrosis and its regression. *Nat. Rev. Gastroenterol. Hepatol.* **18**, 151–166 (2021).
38. Gracia-Sancho, J., Caparrós, E., Fernández-Iglesias, A. & Francés, R. Role of liver sinusoidal endothelial cells in liver diseases. *Nat. Rev. Gastroenterol. Hepatol.* **18**, 411–431 (2021).
39. Xu, M., Wang, X., Zou, Y. & Zhong, Y. Key role of liver sinusoidal endothelial cells in liver fibrosis. *Biosci. Trends* **11**, 163–168 (2017).

Acknowledgements

This work was supported by The National Key Research and Development Program of China (No. 2022YFE0133500), The National Natural Science Foundation of China (No. 32271426), The National High Level Talents Special Support Plan (W. Liu), Thousand Talents Plan of Shaanxi Province (For W. He), “The Young Talent Support Plan” of Xi’an Jiaotong

University (W. Liu and W. He). We thank Instrument Analysis Center of Xi'an Jiaotong University for their assistance with TEM, DLS, FT-IR and XPS analysis. The assistance of proteomic analysis and RNA-seq analysis provided by Tgene Biotech (Shanghai) Co., Ltd. is greatly appreciated.

Author contributions

W.He and W.Liu designed the study and analyzed the data. Y.Liu, L.Zhang, L.Li, W.Yang and J.Li performed the experiments. W.He wrote the manuscript and supervised the study. W.Liu revised the manuscript and supervised the study.

Competing interests

The authors declare no competing interests.

Additional information

Supplementary information The online version contains supplementary material available at https://doi.org/10.1038/s41467-025-59885-x.

Correspondence and requests for materials should be addressed to Wenjia Liu or Wangxiao He.

Peer review information *Nature Communications* thanks Yang He and the other, anonymous, reviewers for their contribution to the peer review of this work. A peer review file is available.

Reprints and permissions information is available at http://www.nature.com/reprints